Open Archive Toulouse Archive Ouverte

OATAO is an open access repository that collects the work of Toulouse researchers and makes it freely available over the web where possible

This is an author's version published in: http://oatao.univ-toulouse.fr/25929

Official URL:

https://doi.org/10.1016/j.jcp.2019.05.005

Any correspondence concerning this service should be sent to the repository administrator: tech-oatao@listes-diff.inp-toulouse.fr

On the use of a friction model in a Volume of Fluid solver for the simulation of dynamic contact lines

H. Si Hadj Mohand [a,b], H. Hoang [c], G. Galliero [b], D. Legendre [a,*]

[a] *Institut de Mécanique des Fluides de Toulouse (IMFT), Université de Toulouse, CNRS - Toulouse, France*
[b] *CNRS/TOTAL/Univ. Pau & Pays Adour/E2S UPPA, Laboratoire des Fluides Complexes et leurs Réservoirs-IPRA, UMR5150, 64000, PAU, France*
[c] *Institute of Fundamental and Applied Sciences, Duy Tan University, 10C Tran Nhat Duat Street, District 1, Ho Chi Minh City 700000, Viet Nam*

ABSTRACT

We consider the implementation of a friction contact angle model in a Navier-Stokes VoF-CSF solver for the simulation of moving contact lines at the nano-scale. A liquid-liquid interface confined in a Couette flow generated by two solid walls moving at the same velocity in opposite directions is considered to discuss the relevance of the friction model. The simulations are compared with a reference case obtained using MD simulations by Qian et al. [46]. We show that the Navier Stokes simulations are able to reproduce the MD simulations for both the interface shape and the velocity field. The appropriate contact line friction is found to be grid convergent and of the same order as the friction measured in MD simulations. A detailed investigation of the interface shape has revealed an auto-similar linear profile in the center of the channel. Close to the wall the interface shape follows the classical Log evolution given by the Cox relation despite the wall confinement.

1. Introduction

Dynamic wetting is encountered in various industrial processes and natural systems [51,3], such as coating [16,24], agrochemical technology [61], printing technology [69], road applications [64] and welding [26]. However, the simulation of moving contact lines is still challenging for numerical simulation. This is mainly due to the intrinsic multi-scale nature of the contact line connecting the three phases. In particular, the classical fluid dynamics theory, i.e. Navier-Stokes equations coupled with no slip boundary conditions, is not consistent to describe the fluids dynamic in the contact line region. It predicts an infinite viscous stress and pressure at the contact line, known as the contact line singularity [32,21]. During the last decades, a lot of work has been carried out to remove this singularity and to accurately model the moving contact line [27,7,10,57]. Both molecular and hydrodynamic approaches have been considered. To tackle the multi-scale aspect of the moving contact line problem, i.e. to be able to interpret experiments [37] or to perform numerical simulations [2,20,59,39,41] of drop size of interest for applications, the interface at large scale is connected to molecular effects at the contact line. The apparent contact angle measured at a hydrodynamic or macroscopic distance L_M from the contact line is linked to the contact line velocity and the microscopic angle θ_m measured at a microscopic distance L_m (Cox [14], Voinov [65]). θ_m is usually supposed to be constant and is commonly set equal to the equilibrium (Young) contact angle θ_Y [22]. However, it has been put in evidence that the microscopic angle θ_m may differ from the static angle θ_Y when the

---

* Corresponding author.
  E-mail address: legendre@imft.fr (D. Legendre).

contact line is moving. To address this problem, the Molecular Kinetic Theory (MKT) gives the microscopic contact angle for a moving contact line considering surface displacements or jump of fluid molecules from adsorption sites localized at the wall [8]. In this model based on the theory of rate processes [29], the contact line fluctuates microscopically around its mean position and fluid molecules located at the wall and sufficiently close to the interface jump from adsorption sites localized at each side of the contact line. When the contact line is static at its equilibrium position, the mean rate of jumps is the same in both forward and backward directions. However, when the contact line is moving, the mean jump rates become asymmetric and yields an excess of jump energy in the moving direction. This excess of energy is compensated by the stress associated to the difference between the static and the microscopic contact angles (the so called uncompensated Young stress) and provides the expression for the contact line velocity relative to the wall as:

$$V_{cl} = 2K_0\lambda\sinh\left(\frac{\gamma\left(\cos\theta_Y - \cos\theta_m\right)}{2nk_BT}\right) \tag{1}$$

where λ and K_0 are the jump length and equilibrium frequency, respectively, k_B is the Boltzmann constant, n is the density of adsorption sites on the solid surface usually considered equal to $1/\lambda^2$ and T is the temperature. From this relation the microscopic moving contact angle θ_m can be expressed as a function of the ratio between the contact line velocity and the jump velocity $K_0\lambda$ of the molecules. When the contact line velocity is much smaller than the jump velocity, the relation can be linearized as

$$\cos\theta_Y - \cos\theta_m = \frac{\xi}{\gamma}V_{cl} \tag{2}$$

with the introduction of a friction coefficient ξ at the contact line that can be expressed as [52]:

$$\xi = \frac{k_BT}{K_0\lambda^3} = \frac{\mu\nu_L}{\lambda^3}\exp\left(-\frac{\gamma\lambda^2(1+\cos\theta_Y)}{k_BT}\right) \tag{3}$$

with ν_L the flow unit volume and μ the dynamic viscosity of the fluid.

A significant number of experiments has been conducted to verify the predictions of the MKT approaches, and their variants, to describe moving contact lines [31,60,33,17,30]. However, classical optical techniques provide only global quantities such as the macroscopic contact angle, the contact line velocity and the radius of spreading droplets [55,48,66]. Thus, access to local quantities close to the contact line (such as the microscopic contact angle) by these techniques is limited and the validation of the approaches is so indirect. Recently, the Atomic Force Microscopy (AFM) has been applied to address moving contact line problems and the microscopic contact angle and the interface shape have been measured at the molecular scale in well controlled conditions [13]. Interestingly, these AFM measurements revealed that the microscopic contact angle is closely related to the contact line velocity as expected from the MKT [13,18].

A complementary route to have access to local information regarding the moving contact line problem in model systems is to use Molecular Dynamics (MD) simulations [35,62,46,15,6,54,40]. These molecular scale simulations are nevertheless restricted to the description of nano-systems. They have shown a good ability to capture the complex interfacial and intermolecular effects occurring within the contact line region. They are useful to test and develop models to describe the moving contact line behavior, e.g. MD simulations have been used to improve the MKT model [15,6,54]. Similarly, Qian and co-workers [46,47], on the basis of MD simulations for liquid-liquid interfaces in contact with an ideal solid surface, developed the Generalized Navier Boundary Condition (GNBC) to describe the (slipping) boundary conditions at the contact line in a continuum approach. They demonstrated that the uncompensated Young stress in a partially wetting case is counterbalanced by viscous and friction dissipations, the latter being expressed as the contact line velocity multiplied by a friction coefficient. In the GNBC model, the contact line velocity relative to the wall is related to the unbalanced Young stress through the relation [46,47]:

$$\beta V_{cl} = -\mu\frac{\partial V}{\partial n} - \sigma_{nx}^Y \tag{4}$$

where β is a slip coefficient and $-\sigma_{nx}^Y$ is the uncompensated Young stress, whose integration over the interface satisfies

$$-\int_{int}\sigma_{nx}^Y dx = \gamma\left(\cos\theta_m - \cos\theta_Y\right) \tag{5}$$

Then, Ren and E [49] have reformulated the GNBC relation to propose the following relation for the unbalanced Young stress

$$\cos\theta_m - \cos\theta_Y = \frac{\beta_{cl}}{\gamma}V_{cl} \tag{6}$$

where β_{cl} is an effective friction coefficient at the contact line accounting for both the contact line friction and the viscous shear. Note that under the present form the GNBC model appears similar to the MKT relation (see Eq. (2)) but strictly
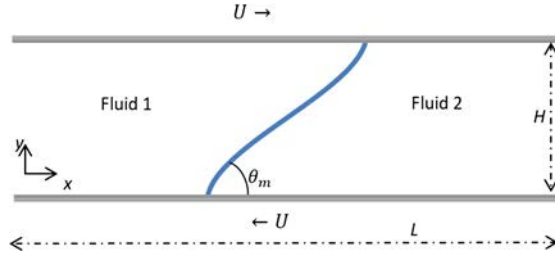
Fig. 1. Couette flow configuration considered here. The two walls are moving with opposite velocities of magnitude U. The reported shape of the interface corresponds to a steady stable solution.

speaking the MKT only considers the contact line friction while the GNBC considers the contact line friction and the viscous shear friction. The GNBC condition has been successfully implemented as boundary condition in continuum simulations by using the diffuse interface (phase field) method based on the Cahn Hilliard model [47,19,5,56,4,42,70], by using the Arbitrary Lagrangian-Eulerian method combined with a finite element method [28] and by using the front tracking method [67,68]. To the best of our knowledge it has not yet been considered in a Volume of Fluid (VoF) - Continuum Surface Force (CSF) formulation.

The aim of this work is to consider the use of a friction model for the simulation of nano-scale moving contact lines using a VoF approach. For this purpose we have selected the steady nano two-phase Couette flows considered by [46,49] because accurate MD results are available for a direct comparison. The main interest of this flow configuration is that the slip at the contact line is steady and perfectly controlled. Indeed, the relative contact line velocity V_{cl} between the contact line and the moving solid wall is equal to the driving velocity U of the solid wall.

The paper is organized as follows. The numerical set-up is described in section 2. The VoF-CSF Navier-Stokes solver used for this study is presented in section 3. The friction contact angle model and its implementation inside a VoF-CSF approach are discussed in section 4. A series of additional validations of the code is proposed in section 5. The numerical simulations of the nano Couette flows considered in this study are detailed in section 6 and the description of the interface shape is reported in section 7.

2. Numerical set-up

A VoF-CSF solver with no interface reconstruction is used for the resolution of the Navier-Stokes equations and the models described in section 4 are considered as boundary condition for the contact line. We aim to (i) demonstrate the ability of a VoF-CSF method to simulate flows at the nano-scale and (ii) to discuss the performances of the different models when used for predictive simulation of moving contact lines. To make relevant the comparison and the discussion, we consider the two-phase Couette flow shown in Fig. 1. A cartesian system of coordinates (e_x, e_y) is used. The walls are parallel to the x-direction and separated by the distance H. They are moving with opposite constant speed of magnitude U along the x-direction. Two immiscible liquids of same density $\rho = \rho_1 = \rho_2$ and same viscosity $\mu = \mu_1 = \mu_2$ are considered. The interface between the two fluids is described with a constant surface tension γ. A plane interface is initially imposed perpendicular to the walls making an initial contact angle of 90°. This flow is very difficult to carry out experimentally [63] but it has the great advantage to provide a 2D steady interface shape with moving contact lines at a constant velocity. The dynamic contact angle with the wall differs slightly from the static contact angle, as shown by MD simulations [46,49]. In addition, the stability of this flow has been studied [34,50,25] and the corresponding transition criteria will be used for the validation of the simulations.

The MD results of Qian et al. [46] will be used as the reference for the comparison with the VoF-CSF simulations. In the MD simulations of Qian et al. [46], interactions between fluid molecules of mass m are modeled by a modified Lennard-Jones potential of the form $4\epsilon \left[(\sigma/r)^{12} - \delta(\sigma/r)^6 \right]$, where r is the distance between two molecules, ϵ and σ are the energy scale and the range of interaction, respectively. $\delta = 1$ for like molecules and $\delta = -1$ for unlike-fluid molecules. Fluid-solid molecular interactions have been described using the same modified Lennard-Jones potential with the energy scale $\epsilon_{fs} = 1.16\epsilon$, the range of interaction $\sigma_{fs} = 1.04\sigma$ and $\delta = \delta_{fs}$ with δ_{fs} defined as: $\delta_{fs} = 1$ for both fluids in the symmetric case while $\delta_{fs} = 1$ for one fluid and $\delta_{fs} = 0.7$ for the other one in the asymmetric case. In the following all parameters are made dimensionless using the mass m of the fluid molecules, the range of interaction σ and the energy scale ϵ. Based on this normalization, the non dimensional parameters of the problem considered in this study are $H = 13.6$, $\rho_1 = \rho_2 = 0.81$, $\mu_1 = \mu_2 = 1.95$ and $\gamma = 5.5$. We consider the two different wetting conditions studied in Qian et al. [46]: a symmetric case corresponding to the equilibrium contact angle $\theta_Y = 90^o$ and an asymmetric case obtained imposing $\theta_Y = 64^o$. The corresponding imposed velocities on the wall are $U = 0.25$ and $U = 0.2$, corresponding to capillary numbers $Ca = 0.089$ and $Ca = 0.071$, respectively. From their MD simulations, Qian et al. [46] deduced the slip lengths values $\ell_1 = \ell_2 = 1.625$, and $\ell_1 = 1.625$, $\ell_2 = 3.67$, for the symmetric and asymmetric configurations, respectively. The values are reported in Table 1.

In Qian et al. [46], the domain of fluid 2 is initially introduced between two domains of fluid 1 to make possible the use of periodical conditions. It results the existence of two interfaces in the computational domain. Here only one interface is simulated and the exact one phase Couette flow solution

Table 1
Values of the slip length ℓ considered in this work.

Name	Symmetric case ($\theta_Y = 90^o$)	Asymmetric case ($\theta_Y = 64^o$)	Reference
$\ell_1 - \ell_2$	$1.625 - 1.625$	$1.625 - 3.67$	Qian et al. [46]
$\ell_{1,VoF} - \ell_{2,VoF}$	$1.22 - 1.22$	$1.42 - 3.21$	Adapted value

$$V_i(y) = \frac{2y}{H + 2\ell_i} U \tag{7}$$

is imposed for the two fluids as boundary condition at the inlet and outlet of the domain located far from the interface. As a consequence the domain length L has been reduced compared to Qian et al. [46]. The effect of the domain length L (i.e. the imposed boundary condition) has been checked by comparing $L = 136$ and $L = 68$, showing a maximum difference between the two solutions less than 0.5%. The domain length considered in the following is $L = 68$.

The computational domain of size $L \times H$ is described using a regular grid $4N \times N$ where N is the number of cells in the direction normal to the moving walls. Different grids made with $N = 32, 64, 128$ and 256 will be used in the following. For all considered grids, the slip zone will be fully resolved. The maximum grid size considered, $\Delta = 0.425$ for $N = 32$, is three times smaller than the minimum slip length that will be considered here. For the more resolved simulations ($N = 256$), the slip zone will be described by more than 20 cells.

3. The Navier-Stokes VoF solver

3.1. 1-Fluid system of equation

The Navier-Stokes simulations are performed using the incompressible Volume of Fluid (VoF) solver implemented in the JADIM code [20,39]. The VoF function C ($C = 1$ in fluid 1 and $C = 0$ in fluid 2) is transported by

$$\frac{\partial C}{\partial t} + V \cdot \nabla C = 0 \tag{8}$$

where $V = CV_1 + (1 - C)V_2$ represents the one-fluid velocity field. The interface is not reconstructed in our VoF approach. An accurate transport algorithm [11] based on FCT (Flux-Corrected-Transport) schemes [71] is used to keep the numerical interface thickness δ_n of about 2-3 grid cells.

Under the assumption of Newtonian incompressible fluids within isothermal conditions and without phase change, the conservation equations of mass and momentum take the following forms:

$$\nabla \cdot V = 0 \tag{9}$$

$$\rho \left(\frac{\partial V}{\partial t} + V \cdot \nabla V \right) = -\nabla P + \nabla \cdot \Sigma + g + F_\gamma \tag{10}$$

where $\rho = C\rho_1 + (1 - C)\rho_2$ is the fluid density, $P = CP_1 + (1 - C)P_2$ is the pressure and the viscous stress tensor is $\Sigma = \mu \left(\nabla V + \nabla^T V \right)$ with $\mu = C\mu_1 + (1 - C)\mu_2$. F_γ is the capillary contribution, given by:

$$F_\gamma = \gamma \nabla \cdot n_I \, n_I \delta_I \tag{11}$$

where γ is the interfacial tension between the two phases, $n_I = \nabla C / \| \nabla C \|$ is the unit vector normal to the interface pointing into fluid 1 and δ_I denotes the delta distribution function of the interface.

The system of equations (8)-(10) is discretized using the second order finite volume method. A staggered mesh is used consisting in locating the VoF function C and the pressure P in the center of the control volume while the velocity components are located normal to the faces of the control volume. Time advancement is achieved through a third order Runge-Kutta method for the advective and source terms and the Crank-Nicolson method is used for the viscous stress. The incompressibility is satisfied at the end of each time step through a projection method.

Boundary conditions for the VoF function C, are required on the boundaries of the domain with non zero normal velocities. The value of C is imposed at the inlet and outlet of the domain to $C = 1$ (fluid 1) and $C = 0$ (fluid 2), respectively. In the following, the liquid-liquid interface is defined by $C = 0.5$. The corresponding contact line position x_{cl} and velocity V_{cl} on each wall are determined by a second order linear interpolation at the interface location ($C = 0.5$). Considering the situation where the interface is located between the cell i and $i + 1$, i.e. $C_i \geq 0.5$ and $C_{i+1} \leq 0.5$, the contact line position and velocity relative to the bottom moving wall are calculated as

$$x_{cl} = \frac{(0.5 - C_{i+1})x_i + (C_i - 0.5)x_{i+1}}{C_i - C_{i+1}}, \tag{12}$$

$$V_{cl} = U + \frac{(0.5 - C_{i+1})V_i + (C_i - 0.5)V_{i+1}}{C_i - C_{i+1}} \tag{13}$$

where V_i is here the tangential fluid velocity at the wall. The value of V_{cl} is determined at each time step and is used to calculate the instantaneous value of the contact angle with one of the models considered in this study. The contact angle between the interface and the wall is imposed through the calculation of the Capillary contribution as described in the following section.

3.2. Capillary contribution

The capillary contribution in the momentum equation is solved using the classical Continuum Surface Force (CSF) approach [12]:

$$F_\gamma = \gamma \nabla \cdot \left(\frac{\nabla C}{|\nabla C|} \right) \nabla C \tag{14}$$

A well known problem of this formulation is the generation of spurious currents [36,45,1]. In order to decrease spurious currents intensity, a classical solution consists in calculating the surface curvature and the normal from a smoothed distribution $\hat{C}$ [12]. The smoothed distribution is $\hat{C} = \hat{C}^m$ at time $(n + 1/2)\Delta t$ where $\hat{C}^m$ is obtained after m iterations. For 2D simulations on a regular grid as considered in this work:

$$\hat{C}_{i,j}^{n_f} = \frac{3}{4}\hat{C}_{i,j}^{n_f-1} + \frac{1}{16}\left(\hat{C}_{i+1,j}^{n_f-1} + \hat{C}_{i-1,j}^{n_f-1} + \hat{C}_{i,j+1}^{n_f-1} + \hat{C}_{i,j-1}^{n_f-1} \right) \tag{15}$$

with $n_f = 1, ..., m$ and $\hat{C}^0$ being initialized with $C^{n+1/2}$. Following Dupont and Legendre [20], the curvature and the normal involved in the capillary term, are obtained with two different values for m, $m_\kappa = 12$ and $m_L = 6$, respectively. The corresponding spurious currents intensity has been characterized and their maximum magnitude evolve as $0.004\gamma/\mu$ [20], in agreement with other codes using the Brackbill's formulation. The corresponding spurious current capillary number is much smaller than the capillary numbers considered in this work, indicating that spurious currents are not expected to induce any perturbation at the interface and on the velocity field.

Considering the finite volume method used for the discretization of the equations, the surface tension contribution integrated in a control volume Ω is expressed as

$$\int_\Omega F_\gamma d\Omega = \gamma \left(\int_V \text{div} \frac{\nabla C}{\| \nabla C \|} dV \right) \nabla C \tag{16}$$

where the divergence term corresponding to the curvature is converted to a surface integral. This term is then evaluated as fluxes of the interface normal $n_I = \nabla C/\| \nabla C \|$ at the surface Γ of Ω:

$$F_\gamma \Omega = \gamma \left(\int_\Gamma n_I \cdot n_\Gamma d\Gamma \right) \nabla C \tag{17}$$

In relation (17) the term in brackets is the curvature and ∇C indicate the direction and location of the imposed capillary contribution. The contact angle made by the interface with the wall is used as a boundary condition in the calculation of the capillary term (14) in the momentum equation. To illustrate this, let's consider a control volume Ω used to calculate the velocity in the x-direction and containing the contact line (i.e. $0 < C < 1$). The contribution of the contact line to the momentum balance in Ω comes from the south face Γ_{South}:

$$F_{\gamma, x, South} \Omega = \gamma \, n_I \cdot n_\Gamma \, \Gamma_{South} \nabla C \cdot e_x \tag{18}$$

where the normal of the south face is $n_\Gamma = -e_y$ and the area is $\Gamma_{South} = \Delta$. The angle θ_m made between the interface and the wall imposes

$$n_I \cdot e_y = \cos \theta_m \tag{19}$$

so that the contact line contribution to the momentum in Ω is

$$F_{\gamma, x, South} \Omega = -\gamma \cos \theta_m \Delta \nabla C \cdot e_x \tag{20}$$

The friction model proposed for the moving contact angle θ_m is presented in the next section. Time and grid convergence and additional validations are reported in section 5.

4. The friction model

A stated before, the objective of this work is to introduce a friction model within a VoF-CSF solver for solving nanoscale moving contact lines. As presented in the introduction the uncompensated Young stress needs to be compensated by an additional friction induced by the motion of the contact line. This friction has two effects that need to be correctly introduced in the simulations: (i) the shear is enhanced at the contact line on the wall and (ii) the angle θ_m made between the interface and the wall is reduced compared to its equilibrium value θ_Y. In addition the Navier condition [43] is applied on the walls. For a wall moving with velocity U, the slip velocity V_i^{slip} of fluid i ($i = 1, 2$) on the wall writes

$$V_i^{slip} = V_i - U = \ell_i \frac{\partial V_i}{\partial y} \tag{21}$$

where ℓ_i is the wall slip length of fluid i, V_i is the velocity of fluid i parallel to the wall and y is the coordinate in the direction normal to the wall.

As discussed in the introduction some friction needs to be introduced at the contact line. Two possible ways are now examined adopting a numerical point of view:

- By the use of a MKT - GNBC like formulation

$$\cos \theta_Y - \cos \theta_m = \frac{\xi}{\gamma} V_{cl} \tag{22}$$

- By the use of an additional viscous friction τ_{cl} at the contact line:

$$\tau_{cl} = \mu_{cl} \frac{\partial V}{\partial y} \tag{23}$$

In order to select the appropriate way to introduce the friction model in a VoF-CSF formulation, let us consider their respective contributions to the momentum balance at the contact line. To simplify the discussion we focus on the bottom wall (south boundary condition). When the wall has no motion ($U = 0$), the angle made by the interface is the static angle $\theta_m = \theta_Y$ and the friction is then zero. As a consequence, the only contribution from the wall to the momentum balance comes from the capillary term contribution $F_{\gamma, x, South} \Omega$ on the south face Γ_{South} given by equation (20). The total contribution of this term over the interface thickness δ_n is

$$\sum_{int} F_{\gamma, South} \Omega \sim - \int_{int} \gamma \cos \theta_Y \frac{\partial C}{\partial x} dx = \gamma \cos \theta_Y \tag{24}$$

Interestingly this term is independent on the numerical thickness δ_n of the interface. It is balanced by the capillary contribution from the other faces of Ω and by the static pressure resulting in the Laplace pressure jump at the interface and an interface shape minimizing the surface energy and satisfying the imposed angle at the wall [20,39].

We now consider the case of a moving contact line. The contact angle is now θ_m. The normal velocity of the south face Γ_{South} being zero, the convective flux is zero. Thus, the contribution of the contact line to the momentum balance on Γ_{South} may include an additional friction τ_{cl}:

$$F_{\gamma, x, South} \Omega + \tau_{cl} \Delta = \left(-\gamma \cos \theta_m \nabla C \cdot e_x + \mu_{cl} \frac{\partial V}{\partial y} \right) \Delta \tag{25}$$

and the integral over the interface thickness becomes

$$F_{\gamma, x, South} \Omega + \tau_{cl} \Delta = \gamma \cos \theta_m + \mu_{cl} \frac{\partial V}{\partial y} \delta_n \tag{26}$$

δ_n being typically of the order of 2-3 grid size Δ, a formulation based on a viscous like contribution τ_{cl} results in a grid dependent contribution at the interface. However, a formulation through $\cos \theta_m$ using a MKT-GNBC like expression (Eq. (22)) provides a contribution to the momentum equation independent of the grid size. As a consequence, the MKT - GNBC like formulation given by Eq. (22) combined with the Navier slip condition (Eq. (21)), will be introduced in the VoF-CSF method. The use of this model requires the value of the static contact angle θ_Y and the value of the contact line friction ξ. The relevant value for ξ will be discussed in section 6.

5. Preliminary tests

The Navier-Stokes solver of JADIM has been intensively validated for both 2D and 3D simulations. The VoF approach associated with the simulation of moving contact lines has been detailed in [20,39] where numerous validations can be found related to static shape of drops on surface as well as spreading or sliding drops. We report here the grid and time convergence of the simulation using the proposed friction model and two additional test cases relevant for the present study.
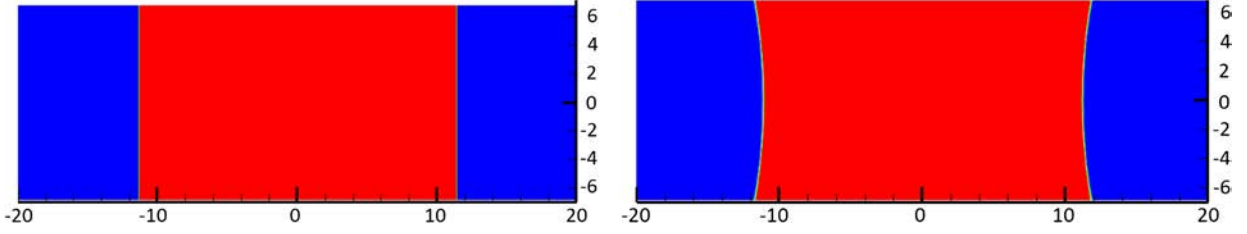
Fig. 2. Liquid drop confined between two static walls. (Left) initial condition. (Right) Stabilized shape ($t = 100$).
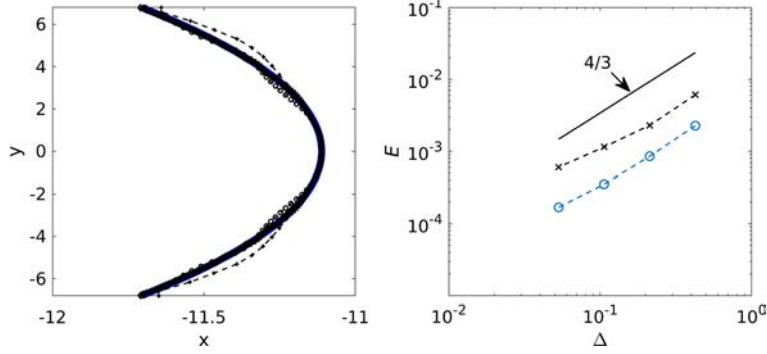

Fig. 3. Liquid drop confined between two static walls. (Left) Comparison between the numerical simulations at $t = 100$ and the exact shape: $*$ $N = 32$, $\circ$ $N = 64$, $\times$ $N = 128$ and $\diamond$ $N = 256$. (Right) Evolution of the errors E_1 ($\circ$) and E_∞ ($\times$) as a function of the grid refinement Δ.

We first consider the static shape of a drop confined between two walls. Then, we study the grid and time convergence for the code using friction model for the simulation of the Couette flow considered in this study. Finally, we investigate the transition between stable and unstable interface shape for the configuration considered in this work and described in section 2.

5.1. Shape of a drop confined between two static walls

The geometry configuration considered for this test is close to the one presented in Fig. 1. A volume of fluid 2 initially delimited by two vertical interfaces with fluid 1 is introduced in the middle of the channel as shown in Fig. 2 (left) forming initial contact angles of 90° with the walls. A constant contact angle $\theta_m = 80^o$ is imposed on the two walls. Due to the imposed contact angle, the system stabilizes to form two concave interfaces of circular shape with radius $R = H/\cos\theta$ as shown in Fig. 2 (right).

The simulations performed with the grids $N = 32$, 64, 128 and 256 are compared in Fig. 3 (left) at time $t = 100$ with the exact circular shape. The error between the numerical position x^Δ and the exact position x^{TH} is measured using the normalized maximum difference E_∞ and the normalized mean difference E_1 defined as:

$$E_\infty = \frac{1}{H} \max_i \left| x_i^\Delta - x_i^{TH} \right|, \quad E_1 = \frac{1}{NH} \sum_i \left| x_i^\Delta - x_i^{TH} \right| \tag{27}$$

The errors E_∞ and E_1 are reported in Fig. 3 (right) as function of the grid refinement Δ. The figure clearly shows a grid convergence of order $\Delta^{4/3}$ between Δ and Δ^2 for both E_∞ and E_1. The same order of convergence is observed when varying the imposed contact angle θ_Y. The numerical discretization scheme for the Navier-Stokes solver in JADIM being second order, the reduction of the order of the grid convergence is attributed to the smoothing procedure applied to C for the calculation of the capillary contribution F_γ.

5.2. Time and grid convergence for the friction model

We report in this section time and grid convergence tests when using the friction model. The convergence tests are performed for the simulation of the 2D Couette flow considered in this study (see Fig. 1). For clarity only the tests performed with the friction coefficient $\xi = 1.7$ are shown. Very similar results were observed when considering other friction coefficients.

We first consider the effect of the time step on the solution. The normalized time step is varied from $\Delta t = 5 \times 10^{-4}$ to $\Delta t = 1.5 \times 10^{-2}$. The grid is made with $N = 64$. The stabilized interface position at time $t = 120$ is reported in Fig. 4 for different time steps. A clear convergence is observed. We introduce the error $E_1^{\Delta t}$ as the normalized mean difference
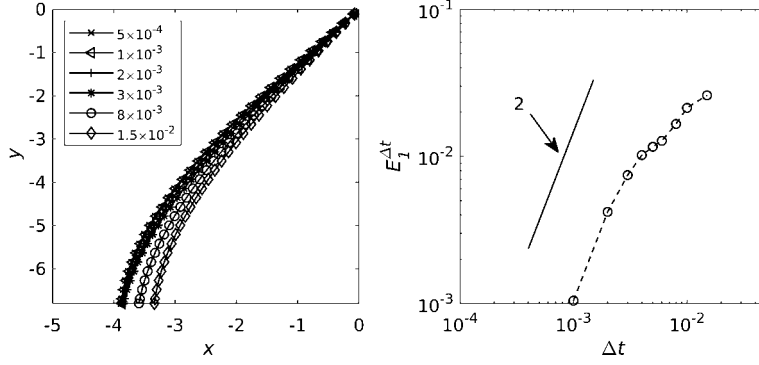
Fig. 4. Time convergence performed for the friction model for $N = 64$ with the friction coefficient $\xi_{cl} = 1.7$. (Left) Interface position for the different time steps at $t = 120$. (Right) Normalized error $E_1^{\Delta t}$ as function of the time step Δt.
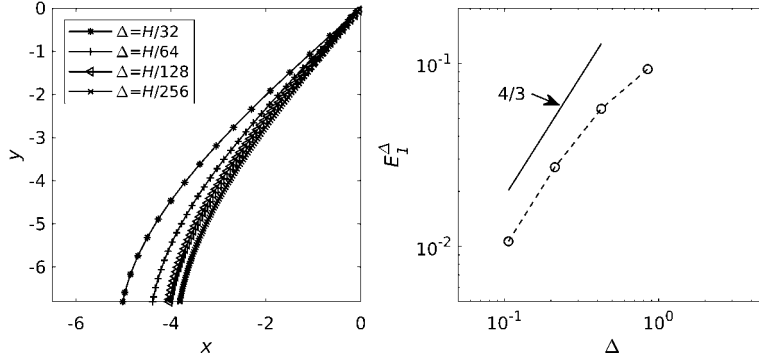

Fig. 5. Grid convergence performed for the friction model with $\xi = 1.7$ with $\Delta t = 2 \times 10^{-3}$. (Left) Interface shape for the different grids. (Right) Evolution of the mean normalized error E_1^{Δ}.

between the solution obtained for Δt and the solution of reference obtained for the smallest time step considered $\Delta t = 5 \times 10^{-4}$:

$$E_1^{\Delta t} = \frac{1}{NH} \sum_i \left| x_i^{\Delta t} - x_i^{\Delta t = 5 \times 10^{-4}} \right| \tag{28}$$

The evolution of $E_1^{\Delta t}$ with Δt reported in Fig. 4 shows that the overall numerical model is second order convergent in time.

The grid convergence is now considered. The number of cells N is varied from 32 to 256. For all the simulations the time step is set to $\Delta t = 2 \times 10^{-3}$ and the simulation time is $t = 120$. This time step ensures time convergence for all the meshes considered. As shown in Fig. 5, the simulation converges when decreasing the grid size. The mean normalized error E_1^{Δ} is defined using the solution obtained for the smallest grid spacing, i.e. $\Delta = H/256$:

$$E_1^{\Delta} = \frac{1}{NH} \sum_i \left| x_i^{\Delta} - x_i^{H/256} \right| \tag{29}$$

The evolution of E_1^{Δ} is reported as a function of the grid spacing Δ in Fig. 5. The time evolution of the capillary number and the viscous shear rate profile at the wall are also shown in Fig. 6 for the different grids tested. These plots clearly indicate that the grid convergence is ensured for all the reported quantities. The interface shape appears to be more sensitive to the mesh refinement and the convergence rate is then $\Delta^{4/3}$. This point will be further discussed in section 5.1.

5.3. Transition from stable to unstable 2D two-phase Couette flow

This last test case is related to the stability of the 2D two-phase Couette flow considered here. This flow configuration is known to present steady or unsteady solutions depending on the velocity imposed on the walls. A steady interface position can be observed as long as the entrainment of the interface by the shear flow can be balanced by the capillary repelling force [34,50,63,25], i.e. $\mu U/H \sim \gamma/H$. It results a critical value for the capillary number $Ca = \mu U/\gamma$. Steady solutions are then observed if the capillary number is smaller than a critical value Ca^*. When $Ca > Ca^*$ the repelling capillary force can not resist to the entrainment of the two contact lines and the interface is continuously elongated. This is illustrated in Fig. 7
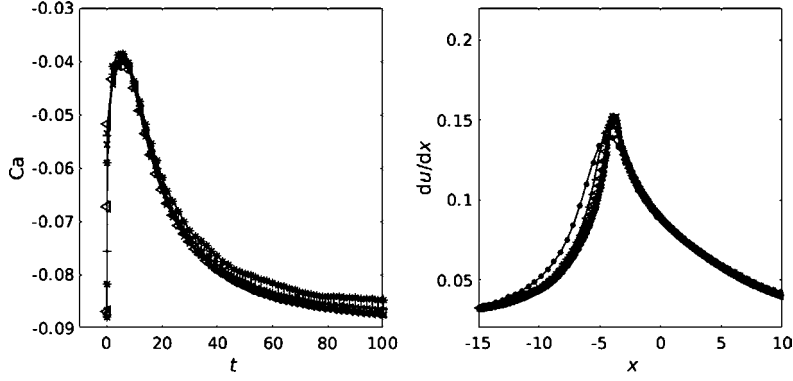
Fig. 6. Grid convergence performed for the friction model with $\xi = 1.7$ with $\Delta t = 2 \times 10^{-3}$. (Left) Time evolution of the contact line capillary number $Ca = \mu V_{cl}/\gamma$ for the different grids. (Right) Velocity gradient at the wall.
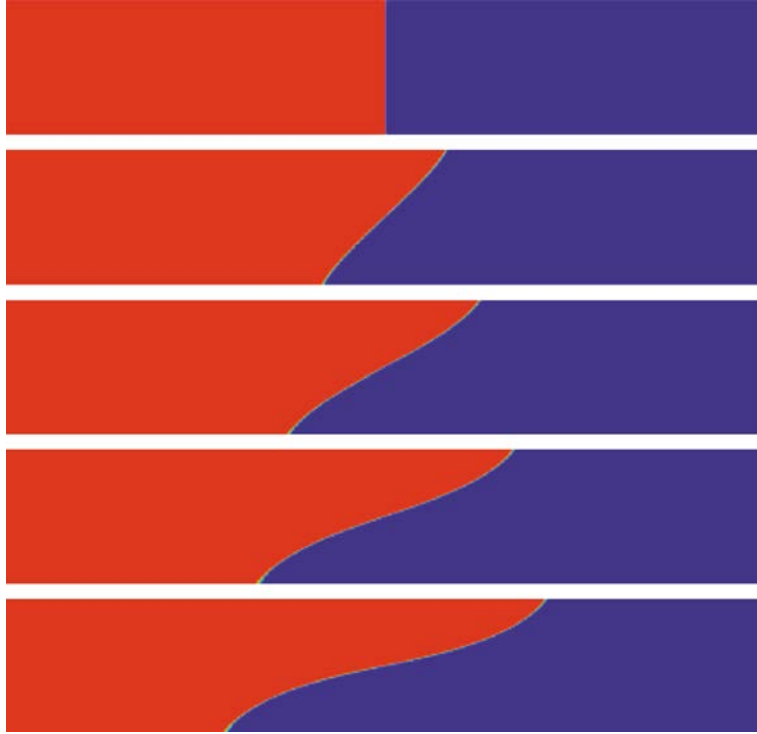

Fig. 7. Successive interface shapes for a typical unsteady situation. From top to bottom $t = 0, 2, 4, 6$ and 8. The imposed contact angle is constant $\theta_m = 90^o$ and the normalized slip are $\ell_1/H = \ell_2/H = 0.089$.

where the interface shape is shown at different time steps when imposing a fixed contact angle $\theta_m = 90^o$ and a normalized slip $\ell/H = 0.089$ for the two fluids.

The critical Capillary number Ca^* depends on both the ratio ℓ/H and the imposed contact angle θ_m [34,50,25]. To determine the transition between stable and unstable situations, simulations are conducted for different imposed contact angles θ_m while imposing a constant slip $\ell/H = 0.089$. The corresponding values of Ca^* are reported in Fig. 8. They are compared to the critical capillary number obtained with the quasi-parallel approximation proposed by Jacqmin [34]. We have solved the system of equations (Eq. 2.7b-2.9 of Jacqmin [34]) using a first order center Euler scheme. The assumption of a quasi-parallel flow induces a solution valid for plane interfaces making the solution a priori valid for small contact angle θ_m with the wall. As shown in Fig. 8 the agreement between the Navier-Stokes simulations and the quasi-parallel approximation is very good for small angles. Then, the difference increases and the quasi-parallel approximation is shown to over predict the transition in agreement with the comparison made in Jacqmin [34] with phase field simulations. However, the prediction given by the quasi-parallel approximation remains in reasonable agreement even at large contact angle.
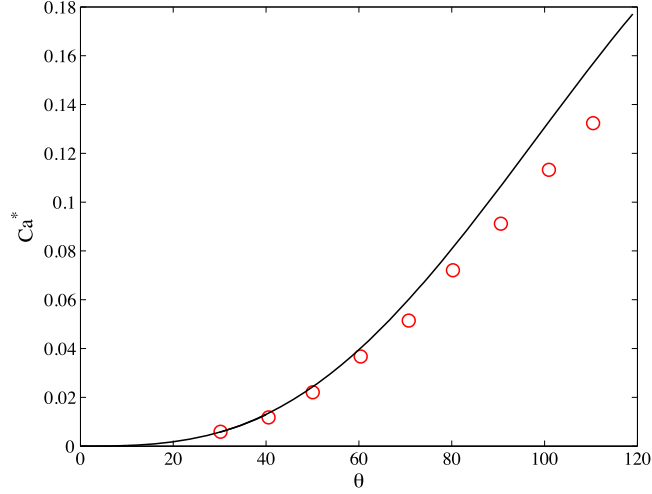
Fig. 8. Critical capillary number as function of the imposed contact angle θ_m with $\ell_1/H = \ell_2/H = 0.089$. ○ Numerical results, (continuous line) the parallel flow solution from Jacqmin [34].
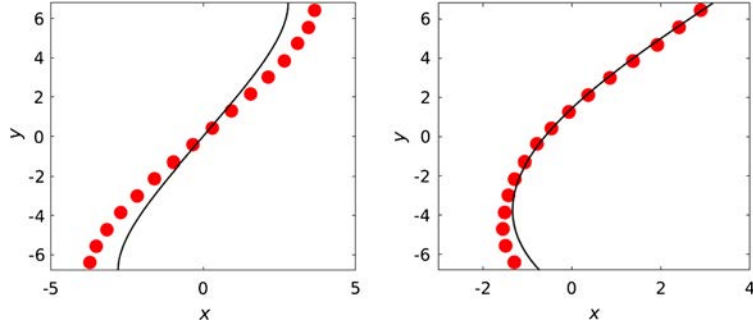

Fig. 9. Interface shape when using the static contact angle model for (left) the symmetric case $\theta_Y = 90^o$ with $\ell_1 = \ell_2 = 1.625$ and (right) for the asymmetric case $\theta_Y = 64^o$ with $\ell_1 = 1.625$ and $\ell_2 = 3.67$. MD simulations are reported using circles.

6. Impact of the friction model

6.1. Simulation with a static contact angle

We first simulate the 2D Couette flow described in Fig. 1 by imposing the static contact angle, so no contact line friction is imposed ($\xi = 0$). The capillary force on the wall is thus calculated with

$$\theta_m = \theta_Y \tag{30}$$

The symmetric ($\theta_Y = 90^o$) and asymmetric ($\theta_Y = 64^o$) cases are considered. The Navier slip condition is imposed with the slip lengths deduced by Qian et al. [46] from their MD simulations and reported in Table 1. The grid used for this comparison is made using $N = 256$ and the normalized time step is $\Delta t = 2 \times 10^{-3}$. The simulations are compared to the MD simulation of Qian et al. [46] in Fig. 9.

The static model is able to capture a steady interface shape comparable to the expected one but the slip at the contact is too large to fit the MD results. The difference in the CL position is noticeably underestimated (about 30%) for the symmetric case while a better agreement is observed for the asymmetric case: the difference is about 20% and the bottom wall while a good agreement is observed on the upper wall. This suggests that the static model is not adapted and that an extra friction needs be added at the contact line as discussed in the following section.

6.2. Simulation with the friction model

The friction coefficient can be determined using the MKT formulation given by relation (3). All the required parameters are given in Qian et al. [46]. In their MD simulations the temperature was controlled at $k_B T = 2.8$. The jump length is linked to the adsorption sites density localized at the wall and can be related to the density of the solid ρ_s as $\lambda = \rho_s^{-1/3} =$

Table 2
Values of the friction coefficient ξ considered in this work.

Name	Symmetric case ($\theta_Y = 90^o$)	Asymmetric case ($\theta_Y = 64^o$)	From Eq.	Reference
ξ_{Ren}	3.02	2.18	(33)	Ren and E [49]
ξ_{MKT}	32.8	57.9	(32)	Ramiasa et al. [48]
				Seveno et al. [53]
ξ_{VoF}	1.7	0.7	Adapted value	This work
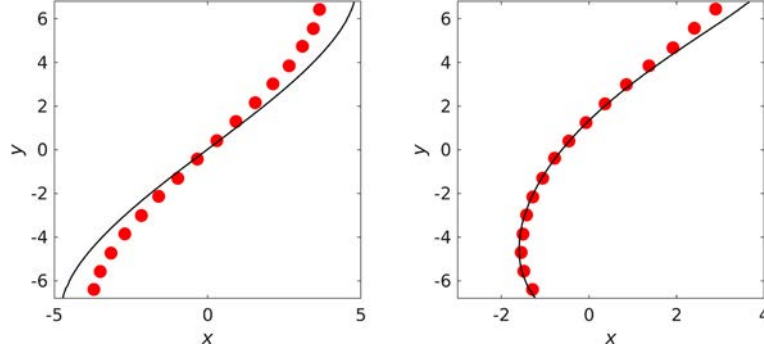
Fig. 10. (left) the symmetric case $\theta_Y = 90^o$ with the friction coefficient $\xi_{Ren} = 3.024$ and for (right) the asymmetric case $\theta_Y = 64^o$ with the friction coefficient $\xi_{Ren} = 2.18$. MD simulations are reported using red circles.

0.813. Note that a very close value is obtained by considering λ as the smallest distance between two wall atoms, i.e. $\lambda = (4/\rho_s)^{1/3}/\sqrt{2} = 0.913$. The jump frequency for a fluid i displacing its vapor is [6]

$$K_{0,i} = \frac{k_B T}{\mu_i \nu_i} \exp\left(-\frac{\gamma \lambda^2 (1 + \cos\theta_Y)}{k_B T}\right) \tag{31}$$

where the unit flow volume of the fluid is taken as $\nu_i = 1/\rho_i$. The corresponding value of the jump frequencies are $K_{0,1} = K_{0,2} = 0.32$ and $K_{0,1} = K_{0,2} = 0.18$ for the symmetric ($\theta_Y = 90^o$) and the asymmetric cases ($\theta_Y = 64^o$), respectively. When considering an interface between two fluids, as in the case considered here, the effective friction is then [48,53]

$$\xi = \xi_1 + \xi_2 \tag{32}$$

where ξ_i is the friction of fluid i given by Eq. (3) with the jump frequency given by Eq. (31). The corresponding values for the normalized friction coefficients are $\xi_{MKT} = 32.8$ and $\xi_{MKT} = 57.9$ for the symmetric and the asymmetric cases, respectively.

The contact line friction can also be determined with the MD simulations of Ren and E [49]. They consider that the friction at the contact line is composed of viscous and frictional parts. Here, the Navier slip condition, i.e. the viscous contribution, is imposed on the entire wall, including the contact line region. Hence only the frictional part reported by Ren and E [49] needs to be considered. It is given by

$$\xi_{Ren} = 0.42\delta B \tag{33}$$

where δ is the contact line thickness and B is the fluid friction coefficient. In the asymmetric case, the fluid friction is different in the two fluids and the average value $B = (B_1 + B_2)/2$ is considered. Based on Ren and E [49] we consider $\delta = 6$. Accordingly, the friction coefficients for the symmetric and the asymmetric cases are $\xi_{Ren} = 3.024$ and $\xi_{Ren} = 2.18$, respectively. The values used for the friction in the following simulations are summarized in Table 2.

The friction given by the MKT prediction is not able to provide a steady state for the interface for both the symmetric and the asymmetric configuration. The interface moves continuously entrained by the moving walls as commented in section 5.3 (see Fig. 7). This indicates that the friction predicted by the MKT model is too large and can not be directly introduced in a Navier-Stokes solver. However, a steady interface is obtained when using the friction ξ_{Ren} deduced from MD simulations as shown in Fig. 10. The agreement appears very good for the asymmetric case $\theta_Y = 64^o$ while in the asymmetric case, the friction ξ_{Ren} overestimates the friction required to match with the reference case. This is evidenced by a more important displacement of the contact line resulting in a more deformed interface than observed in the case of reference.

These results indicate that the interface shape seems to be very sensitive to the friction introduced in the contact angle model and this confirms the relevance of the choice of this test case. Despite a small difference between θ_Y and θ_m (around 3°) the position of the contact angle is noticeably impacted. These points are further discussed in the next section.

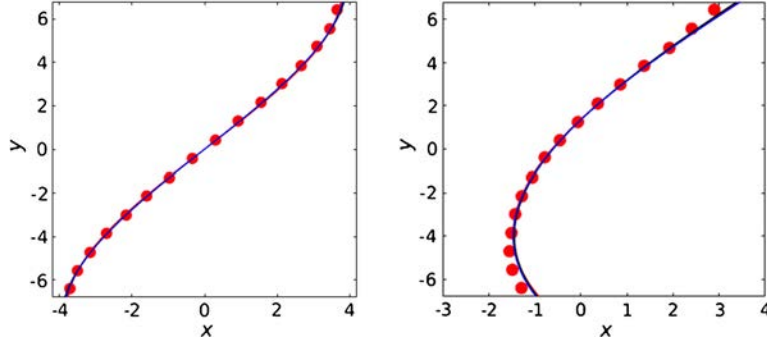**Fig. 11.** Steady state interface shape for (left) the symmetric case $\theta_Y = 90^o$ and (right) the asymmetric case $\theta_Y = 64^o$ for (blue line) the friction model (adjusted friction) and (red line) the static model (adjusted slip length) (see the text). MD simulations are reported using red circles.

6.3. Adapted friction for the VoF-CSF solver

The objective is now to find the correct friction that needs to be used in a VoF-CSF solver to recover the interface shape obtained with the MD simulation. For that purpose we adapt the value of the friction coefficient ξ in order to minimize the difference with the interface shape given by the MD simulation of reference. The reported values correspond to a mean difference less than 0.5%. The slip lengths ℓ_1 and ℓ_2 are unchanged and correspond to the values reported in Table 1. The best agreement with the reference case is obtained for $\xi_{VoF} = 1.7$ and $\xi_{VoF} = 0.7$ for $\theta_Y = 90^o$ and $\theta_Y = 64^o$, respectively. The corresponding interface shapes are shown in Fig. 11. The frictions ξ_{VoF} are one order of magnitude smaller than predicted by the MKT model and of the same order of magnitude as those deduced from MD simulations (see Table 2). Some velocity profiles parallel to the walls are reported in Fig. 12 at different vertical positions and compared with the corresponding profiles from the MD simulations. As shown, the agreement for both cases is found very satisfactory.

Note that, a similar approach can be conducted considering the static contact angle model. Now the contact angle is kept fixed to the static contact angle ($\theta_m = \theta_Y = 90^o$ and $\theta_m = \theta_Y = 64^o$) and we reduce the slip length at the wall to get a better agreement with the reference. The "best" slip lengths are compared in Table 1 with the values deduced from the MD simulation. Both the interface shape (Fig. 11) and the velocity profile (Fig. 12) are now in very good agreement with the MD simulations.

These results clearly indicate that, once calibrated, both the friction model (adjusted friction) and the static model (adjusted slip length) are able to provide good results on both the interface shape (Fig. 11) and the velocity field (Fig. 12). One important conclusion is that Navier-Stokes/VoF/CSF simulations are able to reproduce flows and contact line dynamics at the nano-scale. This is in line with previous findings [49,9,38,57,44] which have shown that hydrodynamics is incredibly consistent to describe liquid flows and interface behavior up to the nano-scale. We also show that it is necessary to consider an adapted boundary condition at the contact line. The two approaches considered here (friction versus slip) seems to be able to be used as boundary conditions in an equivalent way. However the change in the dynamic contact angle is here relatively small (around 3°). We can expect that for larger variations of the dynamic contact angle compared to the static angle, an adjustment of the slip length is not relevant because the correct angle at the wall is not imposed.

6.4. Influence of the grid size on the friction coefficient

The model adjustment reported above were performed for a given grid corresponding to $N = 256$. We now investigate the effect of the grid size on the value of ξ_{VoF} for the friction model and on the slip ℓ_{VoF} for the use of a constant contact angle. The optimal value is determined for each grid following the procedure described above. The corresponding values of the friction and the slip length reported in Fig. 13 converge with the grid refinement. The values are very sensitive to the grid for small resolutions, i.e. $N < 100$. For better resolutions, both ξ_{VoF} and ℓ_{VoF} are almost constant.

7. Interface shape

The objective of this section is to focus on the interface shape for different capillary numbers and ratios H/ℓ. The gap H of the channel is increased while keeping unchanged the slip length and the physical properties (see section 2). The values $H = 13.6$, 450 and 2250 are considered corresponding to $H/\ell = 8.37$, 277 and 1385, respectively. The simulations are performed using the friction model with the friction ξ_{VoF} given in Table 2. The domain size is $L = 4 \times H$ for all the cases. The grid size is chosen to ensure that the slip zone is resolved and the grid convergence has also been checked for the new cases considered. The wall velocity is also varied up to the limit of stability of the interface. The interface shape for velocity ranging from $U = 0.03$ to $U = 0.08$ are reported in Fig. 14 for $H = 450$ and $N = 256$. This corresponds to capillary numbers ranging from $Ca = 0.106$ to $Ca = 0.284$ and contact angles given by the friction model varying from $\theta_m = 89.5^o$ to $\theta_m = 88.6^o$. For this case we observed that the onset of the unsteady regime is between $U = 0.08$ and $U = 0.09$, i.e. for

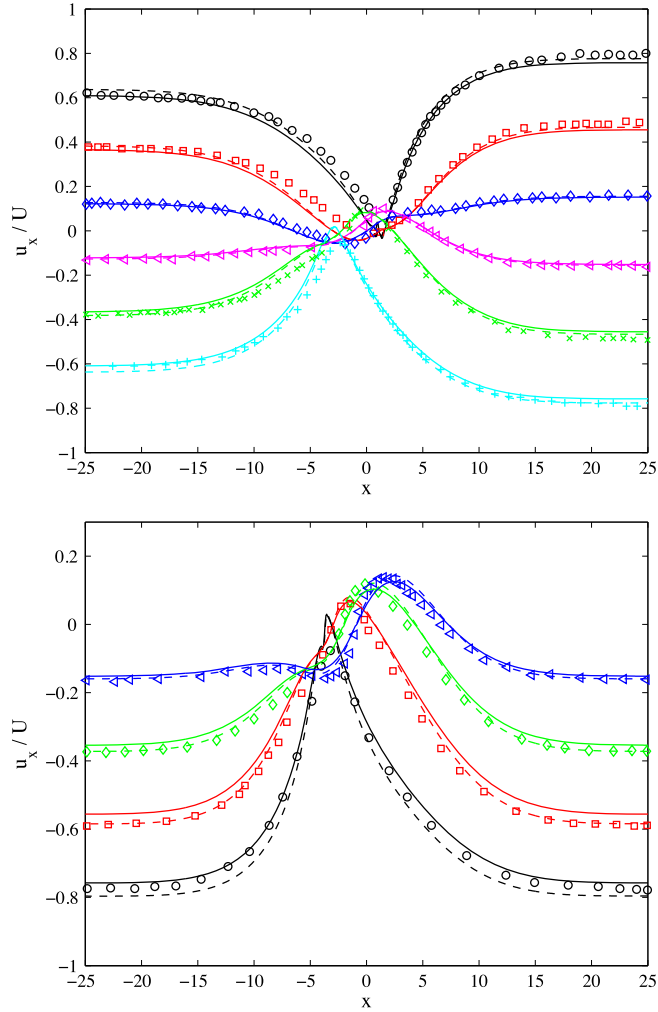**Fig. 12.** Tangential velocity profiles for (top) the symmetric case $\theta_Y = 90^o$ and (bottom) the asymmetric case $\theta_Y = 64^o$. Comparison between the adjusted static model (dashed lines) and friction models (continuous lines) and the MD results (symbols) from Qian et al. [46]: (top) $y = -6.375$ (○); $y = -4.675$ (□); $y = -2.975$ (◇); $y = -1.275$ (△). (bottom): $y = -6.375$ (+); $y = -3.825$ (×); $y = -1.275$ (△); $y = 1.275$ (◇); $y = 3.825$ (□); $y = 6.375$ (○).
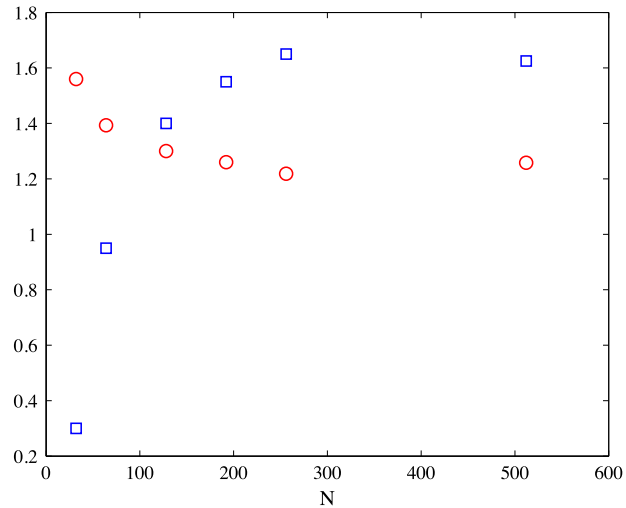

Fig. 13. Influence of the grid size on □ the friction coefficient ξ_{VoF} and ○ the slip length ℓ_{VoF} for the static model. N is the number of cells along the y-direction.

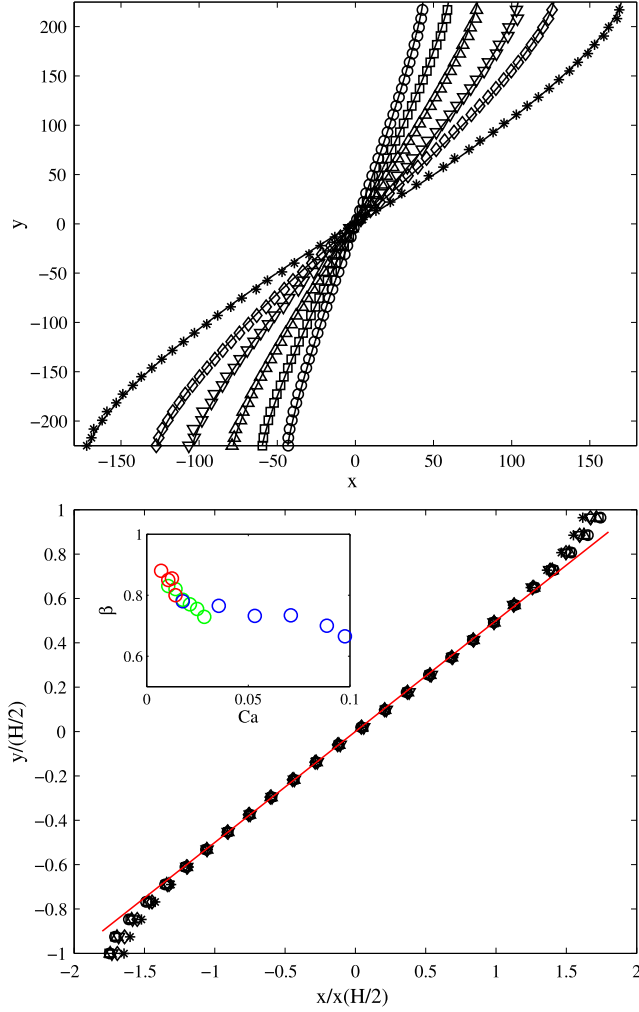**Fig. 14.** (top) Interface shape for $H = 450$ and for wall velocity $U = 0.03$ (○), $U = 0.04$ (□), $U = 0.05$ (△), $U = 0.06$ (▽), $U = 0.07$ (◇) and $U = 0.08$ (⋆). Continuous line Eq. (34). (bottom) Normalized interface shape showing the linear evolution in the channel center. (insert) β versus Ca for (○) $H = 13.6$, (○) $H = 450$ and (○) $H = 2250$.

capillary number between $Ca = 0.284$ and $Ca = 0.319$. As expected, when the capillary number is increased the interface deformation is enhanced.

A detailed inspection shows that the interface shape exhibits an auto-similar behavior in the channel center when varying the wall velocity as reported in Fig. 14. When reporting y normalized by $H/2$ as a function of x normalized by the interface abscise at $y = H/2$ (noted $x(H/2)$) the interface shapes almost collapse and follow a linear shape that can be described with

$$y = \frac{H\beta}{2} \frac{x}{x_{cl}} \tag{34}$$

where x_{cl} is the contact line displacement and the parameter β is a function of Ca as shown in the insert of Fig. 14.

Close to the wall the interface shape depends on both the capillary number and the imposed contact angle. To describe the interface shape in the vicinity of the wall, we consider the evolution of the interface angle $\theta(r)$ made by the interface with the x-axis parallel to the walls. In the reference frame attached to the wall the contact line is a receding (resp. advancing) contact line at the bottom (resp. top) wall for Fluid 2. According to the hydrodynamic model of Cox [14], the interface angle $\theta(r)$ at the distance r to the bottom contact line is given by

$$g(\theta(r), q) = g(\theta_m, q) - Ca \operatorname{Ln}(r/\ell) \tag{35}$$

where $q = \mu_2/\mu_1$ is the viscosity ratio and the function $g(\theta, q)$ is given by
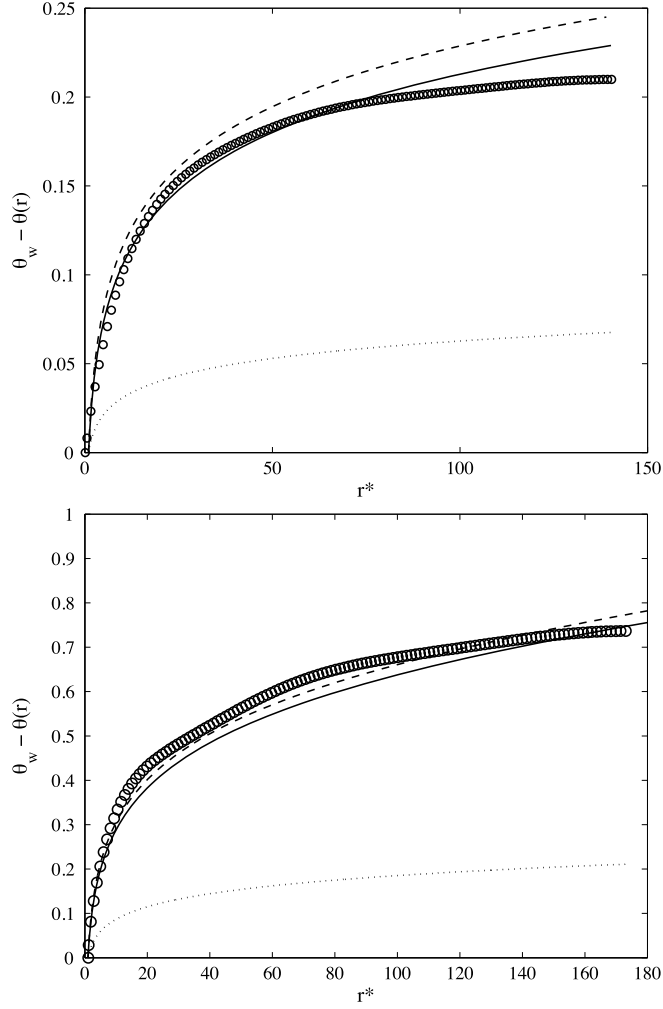
Fig. 15. Variation of the Interface angle $\theta_m - \theta(r)$ as a function of the normalized distance $r^* = r/\ell$ to the contact line for $H = 450$ and Capillary numbers $Ca = 0.106$ (top) and $Ca = 0.284$ (bottom). Continuous line: Cox relation (35) with $g(\theta(r), q)$ given by (36), Dotted line: Cox relation (35) with $g(\theta(r), q)$ given by (37), Dashed line: Cox relation (35) with $g(\theta(r), q)$ given by (38).

$$g(\theta, q) = \int_0^\theta f(\beta, q) d\beta \tag{36}$$

with

$$f(\beta, q) = \frac{q(\beta^2 - \sin^2 \beta)[(\pi - \beta) + \sin \beta \cos \beta] + \left[(\pi - \beta)^2 - \sin^2 \beta\right](\beta - \sin \beta \cos \beta)}{2 \sin \beta \left[q^2(\beta^2 - \sin^2 \beta) + 2q\left(\beta(\pi - \beta) + \sin^2 \beta\right) + ((\pi - \beta)^2 - \sin^2 \beta)\right]}$$

When the contact angle satisfies the condition ($\theta \leq 3\pi/4$) for a liquid displacing a gas ($q = 0$), the function g can be simplified as

$$g(\theta(r), q) \approx \frac{\theta^3}{9} \tag{37}$$

For two liquids this relation remains a good approximation but for smaller angles, typically $\theta \leq \pi/3$ for $q = 1$. Thus, for the range of contact angles considered here the next correction in θ needs to be considered in the expansion [23]

$$g(\theta(r), q) = \frac{\theta^3}{9} - q\frac{\theta^4}{8\pi} + O(\theta^5) \tag{38}$$

These relations are reported in Fig. 15 for $q = 1$ and compared to the numerical simulations for $H = 450$. Two capillary numbers $Ca = 0.106$ and $Ca = 0.284$ have been selected. For clarity the angle variation $\theta_m - \theta(r)$ is reported as a function

of the normalized distance $r^* = r/\ell$ to the contact line. As clearly shown, relation (35) with $g(\theta(r), q)$ given by expression (36) is able to describe the evolution of the angle in the vicinity of the wall despite the confinement imposed by the two walls moving in opposite directions. It is remarkable that relation (35) obtained with a derivation based on matching inner and outer regions through an intermediate region seems to still apply in such a flow configuration. The agreement between numerical results and the Cox relation is improved when the capillary number is decreased. Note that relation (37) often used for the description of dynamic contact lines is far to describe the evolution of the interface shape for two liquids. However, relation (38) appears to be a very interesting approximation to the function $g(\theta(r), q)$. These results indicate that numerical strategies [20,59,39,58] using contact angle models based on the use of the Cox hydrodynamic model (Eq. (35)) remains relevant for such confined flows.

8. Conclusion

We have presented the implementation of a dynamic contact angle model based on the contact line friction in a Navier-Stokes VoF-CSF solver for the simulation of moving contact lines at the nano-scale. The dynamic contact angle model requires the value of the static contact angle and the value of the contact line friction, while the slip length is used to impose a Navier boundary condition. A liquid-liquid interface confined in a Couette flow generated by two walls moving at the same velocity in opposite directions is considered to discuss the relevance of the friction model. The simulations are compared with a reference case obtained by MD simulations [46]. We show that the Navier Stokes simulations are able to reproduce the MD simulations for both the interface shape and the velocity field. The appropriate contact line friction is found to be grid convergent and of the same order as the friction measured in MD simulations while the friction deduced from the MKT model seems not able to provide an appropriate friction for a Navier-Stokes solver as considered here. A detailed investigation of the interface shape has revealed an auto-similar linear profile in the center of the channel. Close to the wall the interface shape is observed to follow the classical Log evolution given by the Cox relation despite the confinement imposed by the walls. Additional MD simulations and appropriate experiments are required to further investigate the friction at a moving contact line. These results will be of importance for the implementation of friction models in Navier-Stokes solvers for the simulations of moving contact lines.

References

[1] T. Abadie, J. Aubin, D. Legendre, On the combined effects of surface force calculation and interface advection on spurious currents within volume of fluid and level set frameworks, Comput. Fluids 297 (2013) 611–636.
[2] S. Afkhami, S. Zaleski, M. Bussmann, A mesh-dependent model for applying dynamic contact angles to vof simulations, J. Comput. Phys. 228 (2009) 5370–5389.
[3] G. Ahmed, O. Arjmandi Tash, J. Cook, A. Trybala, V. Starov, Biological applications of kinetics of wetting and spreading, Adv. Colloid Interface Sci. 249 (2017) 17–36, https://doi.org/10.1016/j.cis.2017.08.004.
[4] F. Bai, X. He, X. Yang, R. Zhou, C. Wang, A finite element method for the numerical solution of the coupled cahn-hilliard and navier-stokes system for moving contact line problems, Int. J. Multiph. Flow 93 (2017) 130–141.
[5] K. Bao, Y. Shi, S. Sun, X.P. Wang, A finite element method for the numerical solution of the coupled cahn-hilliard and navier-stokes system for moving contact line problems, J. Comput. Phys. 231 (2012) 8083–8099.
[6] E. Bertrand, T.D. Blake, J. De Coninck, Influence of solid-liquid interactions on dynamic wetting: a molecular dynamics study, J. Phys. Condens. Matter 21 (46) (2009) 464124.
[7] T. Blake, The physics of moving wetting lines, J. Colloid Interface Sci. 299 (2006) 1–13.
[8] T. Blake, J. Haynes, Kinetics of liquid/liquid displacement, J. Colloid Interface Sci. 30 (1969) 421–423.
[9] L. Bocquet, E. Charlaix, Nanofluidics, from bulk to interfaces, Chem. Soc. Rev. 39 (2010) 1073–1095.
[10] D. Bonn, J. Eggers, J. Indekeu, J. Meunier, E. Rolley, Wetting and spreading, Rev. Mod. Phys. 81 (2009) 739–805.
[11] T. Bonometti, J. Magnaudet, An interface capturing method for incompressible two-phase flows. Validation and application to bubble dynamics, Int. J. Multiph. Flow 33 (2007) 109–133.
[12] J. Brackbill, D. Kothe, C. Zemach, A continuum method for modeling surface tension, J. Comput. Phys. 100 (1992) 335–354.
[13] L. Chen, J. Yu, H. Wang, Convex nanobending at a moving contact line: the missing mesoscopic link in dynamic wetting, ACS Nano 8 (2014) 11493–11498.
[14] R. Cox, The dynamics of the spreading of liquids on a solid surfaces. part 1: Viscous flow, J. Fluid Mech. 168 (1986) 169–194.
[15] J. De Coninck, T. Blake, Wetting and molecular dynamics simulations of simple liquids, Annu. Rev. Mater. Res. 38 (2008) 1–22.
[16] A. Deblais, R. Harich, A. Colin, H. Kellay, Taming contact line instability for pattern formation, Nat. Commun. 7 (2016) 12458.
[17] G. Delon, M. Fermigier, J. Snoeijer, B. Andreotti, Relaxation of a dewetting contact line. part 2. experiments, J. Fluid Mech. 604 (2008) 55–75.
[18] Y. Deng, L. Chen, Q. Liu, J. Yu, H. Wang, Nanoscale view of dewetting and coating on partially wetted solids, J. Phys. Chem. Lett. 7 (2016) 1763–1768.
[19] Y. Di, X.P. Wang, Precursor simulations in spreading using a multi-mesh adaptive finite element method, J. Comput. Phys. 228 (2009) 1380–1390.
[20] J. Dupont, D. Legendre, Numerical simulations of static and sliding drop with contact angle hysteresis, J. Comput. Phys. 229 (2010) 2453–2478.
[21] V.E. Dussan, S. Davis, On the motion of a fluid-fluid interface along a solid surface, J. Fluid Mech. 65 (1974) 71–95.
[22] J. Eggers, Hydrodynamic theory of forced dewetting, Phys. Rev. Lett. 93 (2004) 094502.
[23] R.T. Foister, The kinetics of displacement wetting in liquid/liquid/solid systems, J. Colloid Interface Sci. 136 (1) (1990) 266–282.
[24] P. Gao, L. Li, J. Feng, H. Ding, X.Y. Lu, Film deposition and transition on a partially wetting plate in dip coating, J. Fluid Mech. 791 (2016) 358–383.

[25] P. Gao, X.Y. Lu, On the wetting dynamics in a couette flow, J. Fluid Mech. 724 (2013) R1.
[26] M. Gatzen, T. Radel, C. Thomy, F. Vollertsen, Wetting and solidification characteristics of aluminium on zinc coated steel in laser welding and brazing, J. Mater. Process. Technol. 238 (2016) 352–360.
[27] P.G. de Gennes, Wetting: statics and dynamics, Rev. Mod. Phys. 57 (1985) 827–863.
[28] J.F. Gerbeau, T. Lelièvre, Generalized navier boundary condition and geometric conservation law for surface tension, Comput. Methods Appl. Mech. Eng. 198 (2009) 644–656.
[29] S. Glasstone, K. Laidler, H. Eyring, The Theory of Rate Processes: The Kinetics of Chemical Reactions, Viscosity, Diffusion and Electrochemical Phenomena, McGraw-Hill, New York, 1941.
[30] F. Henrich, D. Fell, D. Truszkowska, M. Weirich, M. Anyfantakis, T.H. Nguyen, M. Wagner, G. Auernhammer, H.J. Butt, Influence of surfactants in forced dynamic dewetting, Soft Matter 12 (2016) 7782–7791.
[31] R. Hoffman, A study of the advancing interface. i. interface shape in liquid-gas systems, J. Colloid Interface Sci. 50 (1975) 228–241.
[32] C. Hu, L. Scriven, Hydrodynamic model of steady movement of a solid/liquid/fluid contact line, J. Colloid Interface Sci. 35 (1971) 85–101.
[33] H. Huppert, The propagation of two-dimensional and axisymmetric viscous gravity currents over a rigid horizontal surface, J. Fluid Mech. 121 (1982) 43–58.
[34] D. Jacqmin, Onset of wetting failure in liquid-liquid systems, J. Fluid Mech. 517 (2004) 209–228.
[35] J. Koplik, J. Banavar, J. Willemsen, Molecular dynamics of poiseuille flow and moving contact lines, Phys. Rev. Lett. 60 (1988) 1282–1285.
[36] B. Lafaurie, C. Nardone, R. Scardovelli, S. Zaleski, G. Zanetti, Modelling merging and fragmentation in multiphase flows with surfer, J. Comput. Phys. 113 (1994) 134–147.
[37] N. Le Grand, A. Daerr, L. Limat, Shape and motion of drops sliding down an inclined plate, J. Fluid Mech. 541 (2005) 293–315.
[38] R. Ledesma-Alonso, D. Legendre, Ph. Tordjeman, Nanoscale deformation of a liquid surface, Phys. Rev. Lett. 108 (2012) 106104.
[39] D. Legendre, M. Maglio, Comparison between numerical models for the simulation of moving contact lines, Comput. Fluids 113 (2015) 2–13.
[40] A. Lukyanov, A. Likhtman, Dynamic contact angle at the nanoscale: a unified view, ACS Nano 10 (2016) 6045–6053.
[41] J. Luo, X. Hu, N. Adams, Curvature boundary condition for a moving contact line, J. Comput. Phys. 310 (2016) 329–341.
[42] J. Luo, X.P. Wang, X.C. Cai, An efficient finite element method for simulation of droplet spreading on a topologically rough surface, J. Comput. Phys. 349 (2017) 233–252.
[43] C. Navier, Mémoire sur les lois du mouvement des fluides, Mém. Acad. R. Sci. Inst. Fr. 6 (1823) 389–440.
[44] P. Poesio, A. Damone, O. Matar, Slip at liquid-liquid interfaces, Phys. Rev. Fluids 2 (2017) 044004.
[45] S. Popinet, S. Zaleski, A front-tracking algorithm for accurate representation of surface tension, Int. J. Numer. Methods Fluids 30 (1999) 775–793.
[46] T. Qian, X.P. Wang, P. Sheng, Molecular scale contact line hydrodynamics of immiscible flows, Phys. Rev. E 68 (2003) 016306.
[47] T. Qian, X.P. Wang, P. Sheng, A variational approach to moving contact line hydrodynamics, J. Fluid Mech. 564 (2006) 333–360.
[48] M. Ramiasa, J. Ralston, R. Fetzer, R. Sedev, Contact line friction in liquid-liquid displacement on hydrophobic surfaces, J. Phys. Chem. C 115 (20) (2011) 24975–24986, https://doi.org/10.1021/jp209140a.
[49] W. Ren, W. E, Boundary conditions for the moving contact line problem, Phys. Fluids 19 (2007) 022101.
[50] M. Sbragaglia, K. Sugiyama, L. Biferale, Wetting failure and contact line dynamics in a couette flow, J. Fluid Mech. 614 (2008) 471–493.
[51] K. Sefiane, M. Shanahan, M. Antoni, Wetting and phase change: opportunities and challenges, Curr. Opin. Colloid Interface Sci. 16 (2011) 317–325.
[52] D. Seveno, T.D. Blake, S. Goossens, J. De Coninck, Predicting the wetting dynamics of a two-liquid system, Langmuir 27 (2011) 14958–14967.
[53] D. Seveno, T.D. Blake, S. Goossens, J. De Coninck, Correction to 'predicting the wetting dynamics of a two-liquid system', Langmuir 34 (2018) 5160–5161.
[54] D. Seveno, N. Dinter, J. De Coninck, Wetting dynamics of drop spreading. new evidence for the microscopic validity of the molecular-kinetic theory, Langmuir 26 (2011) 14642–14647.
[55] D. Seveno, A. Vaillant, R. Rioboo, H. Adão, J. Conti, J. De Coninck, Dynamics of wetting revisited, Langmuir 25 (22) (2009) 13034–13044.
[56] S. Shao, T. Qian, A variational model for two-phase immiscible electroosmotic flow at solid surfaces, Commun. Comput. Phys. 11 (2012) 831–862.
[57] J. Snoeijer, B. Andreotti, Moving contact lines: scales, regimes, and dynamical transitions, Annu. Rev. Fluid Mech. 45 (2013) 269–292.
[58] Z. Solomenko, P. Spelt, P. Alix, A level-set method for large-scale simulations of three-dimensional flows with moving contact lines, J. Comput. Phys. 348 (2017) 151–170.
[59] Y. Sui, P. Spelt, An efficient computational model for macroscale simulations of moving contact lines, J. Comput. Phys. 242 (2013) 37–52.
[60] L. Tanner, The spreading of silicone oil drops on horizontal surfaces, J. Phys. D, Appl. Phys. 12 (1979) 1473–1484.
[61] P. Taylor, The wetting of leaf surfaces, Curr. Opin. Colloid Interface Sci. 16 (2011) 326–334.
[62] P. Thompson, M. Robbins, Simulations of contact-line motion: slip and the dynamic contact angle, Phys. Rev. Lett. 63 (1989) 766–769.
[63] E. Vandre, M.S. Carvalho, S. Kumar, Delaying the onset of dynamic wetting failure through meniscus confinement, J. Fluid Mech. 707 (2012) 496–520.
[64] S. Vassaux, V. Gaudefroy, L. Boulangé, A. Pévère, V. Mouillet, V. Barragan-Montero, Towards a better understanding of wetting regimes at the interface asphalt/aggregate during warm-mix process of asphalt mixtures, Constr. Build. Mater. 133 (2017) 182–195.
[65] O. Voinov, Hydrodynamics of wetting, J. Fluid Dyn. 11 (1976) 714–721.
[66] K. Winkels, J. Weijs, A. Eddi, J. Snoeijer, Initial spreading of low-viscosity drops on partially wetting surfaces, Phys. Rev. E 85 (2012) 055301(R).
[67] Y. Yamamoto, T. Ito, T. Wakimoto, K. Katoh, Numerical simulations of spontaneous capillary rises with very low capillary numbers using a front-tracking method combined with generalized navier boundary condition, Int. J. Multiph. Flow 51 (2013) 22–32.
[68] Y. Yamamoto, K. Tokieda, T. Wakimoto, T. Ito, K. Katoh, Modeling of the dynamic wetting behavior in a capillary tube considering the macroscopic?microscopic contact angle relation and generalized navier boundary condition, Int. J. Multiph. Flow 59 (2014) 106–112.
[69] H.S. Yoon, H.T. Lee, E.S. Kim, S.H. Ahn, Direct printing of anisotropic wetting patterns using aerodynamically focused nanoparticle (afn) printing, Appl. Surf. Sci. 396 (2017) 1450–1457.
[70] H. Yu, X. Yang, Numerical approximations for a phase-field moving contact line model with variable densities and viscosities, J. Comput. Phys. 334 (2017) 665–686.
[71] S. Zalesak, Fully multidimensional flux-corrected transport algorithms for fluids, J. Comput. Phys. 31 (1979) 335–362.